RESEARCH ARTICLE

ADVANCED MATERIALS
www.advmat.de

# Multistep Dissolution of Lamellar Crystals Generates Superthin Amorphous $Ni(OH)_2$ Catalyst for UOR

*Yajie Zhu, Cheng Liu, Shiwen Cui, Zhuorong Lu, Jinyu Ye, Yunzhou Wen, Wenjuan Shi, Xiaoxiong Huang, Liangyao Xue, Juanjuan Bian, Youyong Li, Yifei Xu,* and Bo Zhang**

**Urea oxidation reaction (UOR) is an ideal replacement of the conventional anodic oxygen evolution reaction (OER) for efficient hydrogen production due to the favorable thermodynamics. However, the UOR activity is severely limited by the high oxidation potential of Ni-based catalysts to form $Ni^{3+}$, which is considered as the active site for UOR. Herein, by using in situ cryoTEM, cryo-electron tomography, and in situ Raman, combined with theoretical calculations, a multistep dissolution process of nickel molybdate hydrate is reported, whereby $NiMoO_4{\cdot}xH_2O$ nanosheets exfoliate from the bulk $NiMoO_4{\cdot}H_2O$ nanorods due to the dissolution of Mo species and crystalline water, and further dissolution results in superthin and amorphous nickel (II) hydroxide (ANH) flocculus catalyst. Owing to the superthin and amorphous structure, the ANH catalyst can be oxidized to NiOOH at a much lower potential than conventional $Ni(OH)_2$ and finally exhibits more than an order of magnitude higher current density (640 mA $cm^{-2}$), 30 times higher mass activity, 27 times higher TOF than those of $Ni(OH)_2$ catalyst. The multistep dissolution mechanism provides an effective methodology for the preparation of highly active amorphous catalysts.**

## 1. Introduction

Hydrogen production by electrochemical water splitting is a sustainable, efficient and promising green energy conversion and storage technology, which can greatly alleviate the problems caused by fossil fuels shortage and environmental pollution.[1] However, the anode half-reaction oxygen evolution reaction (OER) of water splitting suffers from a large thermodynamic potential of 1.23 V (versus the reversible hydrogen electrode (RHE)), and the sluggish dynamics that mismatch with the other half-reaction (hydrogen evolution reaction, HER). These problems hinder the practical applications of OER.[2] Therefore, efficient anode reactions are urgently needed for replacement of OER to reduce the consumption for hydrogen production. Among many anodic reactions, the electrochemical urea oxidation reaction (UOR) shows a favorable prospect of energy-related applications because of its low thermodynamic potential (0.37 V).[2b,3] Moreover, urea containing wastewater from industrial and agriculture can be treated simultaneously through UOR.[4]

UOR is a complicated six-electron-transfer process ($CO(NH_2)_2 + 6OH^- \rightarrow N_2 + 5H_2O + CO_2 + 6e^-$) and the reaction kinetics is also slow, which requires high-performance electrocatalysts with good stability to boost the UOR efficiency.[3a,4] Noble metal based catalysts, such as Ti-Pt and Ru-$TiO_2$ were used initially to achieve high activity for UOR, but the high cost and limited resource impede further industrial applications.[3b] Therefore, considerable attention has been devoted to first-row transition metal Ni-based compounds as substitute for noble metal-based catalysts due to their low cost and high intrinsic catalytic activity for UOR.[3b,4,5]

For most studies, the Ni-based UOR catalysts start from the self-oxidation process of $Ni^{2+}$ containing species such as $Ni(OH)_2$ to form $Ni^{3+}$ containing species such as NiOOH, as $Ni^{3+}$ are considered to be the actual active sites for UOR.[3b,6] In particular, Wang et al. has recently proposed a new UOR mechanism that the urea dehydrogenates oxidation on NiOOH is spontaneous.[7] However, the oxidation potential from $Ni^{2+}$ to $Ni^{3+}$ is up to ≈1.36 V, which severely restricted the subsequent oxidation from urea to $N_2$.[5] Therefore, promoting the oxidation of Ni-based catalysts at low potential is crucial for UOR.

Nickel molybdates has been used as precursor for UOR catalyst, as previous studies have shown that Mo and crystalline water in nickel molybdates can be dissolved by alkali, generating amorphous structure containing $Ni^{2+}$ that can be readily oxidized.[8] The degree of dissolution is closely related to the content of

Y. Zhu, S. Cui, Z. Lu, Y. Wen, W. Shi, X. Huang, L. Xue, J. Bian, Y. Xu, B. Zhang
State Key Laboratory of Molecular Engineering of Polymers
Department of Macromolecular Science
Fudan University
Shanghai 200438, P. R. China
E-mail: xyf@fudan.edu.cn; bozhang@fudan.edu.cn

C. Liu, Y. Li
Institute of Functional Nano & Soft Materials (FUNSOM)
Jiangsu Key Laboratory for Carbon-Based Functional Materials & Devices
Soochow University
Suzhou, Jiangsu 215123, P. R. China

J. Ye
State Key Laboratory for Physical Chemistry of Solid Surfaces
Collaborative Innovation Center of Chemistry for Energy Materials and
College of Chemistry and Chemical Engineering
Xiamen University
Xiamen 361005, P. R. China

The ORCID identification number(s) for the author(s) of this article can be found under https://doi.org/10.1002/adma.202301549

DOI: 10.1002/adma.202301549

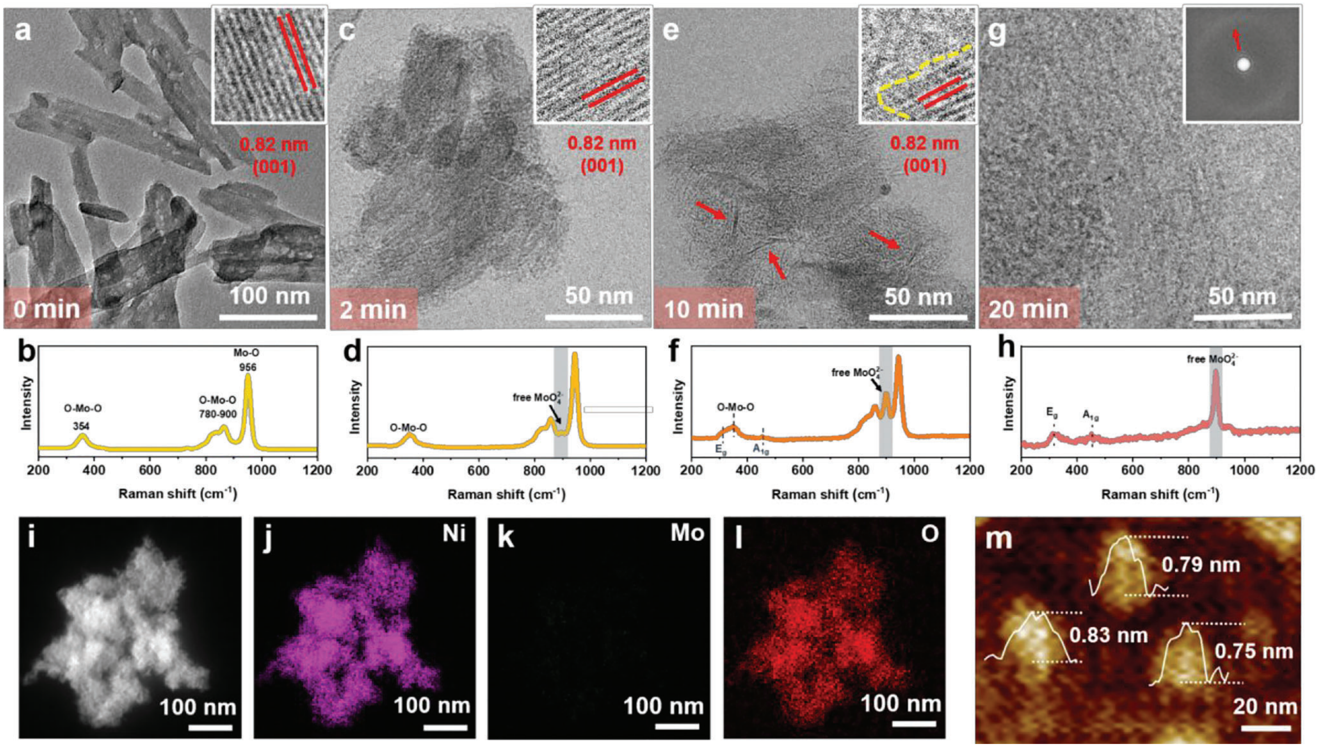

**Figure 1.** Dissolving process of $NiMoO_4 \cdot H_2O$ pre-catalyst. a) HRTEM images of $NiMoO_4 \cdot H_2O$ and the corresponding lattice spacing. b) The Raman spectra of $NiMoO_4 \cdot H_2O$. c–g) CryoTEM images and the corresponding in situ Raman spectra of $NiMoO_4 \cdot H_2O$ dissolved in 0.1 M KOH at t = 2, 10, and 20 min, respectively. Insets of (a), (c), and (e) are magnified images showing the lattice spacing. Inset of (g) is FFT of the image, the vague ring indicated by the red arrow corresponds to the diffraction of vitreous ice. i–l) HAADF-STEM image and corresponding EDS elemental mapping, and m) AFM image and height profiles of the ANH flocculus.

crystalline water. For example, anhydrous $NiMoO_4$ is insusceptible to alkali etching, while most of the Mo species were dissolved in alkali for $NiMoO_4 \cdot 0.75H_2O$ leaving amorphous structures.[8e,9] However, the products remain in the cubic, crystal-like morphology even after alkali etching, which is not favorable for sufficient and swift oxidation of Ni (II) sites at low potential. We propose that with the content of crystalline water in nickel molybdate hydrate further increased, more thorough alkali etching may be achieved, leading to high-surface and more amorphous units, thus reducing the generation potential of $Ni^{3+}$ species.[10]

In this report, we synthesized $NiMoO_4 \cdot H_2O$ which contains more crystalline water than previous reports (1 versus 0.75) in order to generates superthin amorphous $Ni(OH)_2$ catalyst for UOR, and thoroughly investigated the mechanisms underlying its dissolution processes in alkali. Combining theoretical calculations, in situ cryoTEM, cryo-electron tomography (cryoET) and in situ Raman, we revealed a multistep dissolution mechanism of $NiMoO_4 \cdot H_2O$ nanorods involving exfoliation of $NiMoO_4 \cdot xH_2O$ nanosheets and further dissolving, which completely disintegrates the original rod-like morphology and generates superthin and amorphous nickel (II) hydroxide flocculus (ANH). Benefiting from the superthin and amorphous structure, ANH catalyst can be electrooxidized into the high-valent active state at only 1.32 V and achieved more than an order of magnitude higher current density (640 mA cm$^{-2}$), 30 times higher mass activity, 27 times higher TOF than those of $Ni(OH)_2$ catalyst. Besides, we demonstrated the feasible application of ANH in the urea-assisted anion-exchange membrane electrolyzer under harsher operation circumstances for 50 h.

## 2. Results and discussion

### 2.1. Dissolving Process of Nickel Molybdate Hydrate Pre-Catalyst

We synthesized nickel molybdate hydrate ($NiMoO_4 \cdot xH_2O$) pre-catalyst through a one-step microwave method.[11] Scanning electron microscopy (SEM) and transmission electron microscopy (TEM) revealed stacked rod-like crystallites of $NiMoO_4 \cdot H_2O$ pre-catalyst with lengths ranging from 20 to 200 nm (**Figure 1**a; Figure S1, Supporting Information). The results of the High-resolution TEM (HRTEM) and Powder X-ray diffraction (PXRD) confirmed the synthesis of crystalline $NiMoO_4 \cdot xH_2O$. HRTEM images showed a wide lattice spacing of 0.82 nm, which can be assigned to the (001) plane of $NiMoO_4 \cdot xH_2O$ (inset in Figure 1a). As shown in Figure S2 (Supporting Information), the PXRD pattern of $NiMoO_4 \cdot xH_2O$ pre-catalyst powder exhibited three main characteristic peaks at $2\theta$ values of 11.06°, 27.10°, and 29.67°, all of which could be indexed to a standard pattern of $NiMoO_4 \cdot xH_2O$ (JCPDS no. 13–0128). Inductively coupled plasma optical emission spectroscopy (ICP–OES) confirmed that $NiMoO_4 \cdot H_2O$ is composed of Ni and Mo, with a molar ratio of ≈1 (Table S1, Supporting Information). Furthermore, Raman spectroscopy in Figure 1b revealed the typical molybdates peak of 965 cm$^{-1}$, which corresponds to symmetric stretching modes in Mo–O connection.[12] It further showed the peaks of 356 cm$^{-1}$ (asymmetric bending modes in O–Mo–O connections) and 780–900 cm$^{-1}$ (asymmetric stretching modes in O-Mo-O connections).[12] The percentage of water contents was confirmed by thermogravimetric analysis (TGA) (Figure S3, Supporting Information), indicating that the molecular formula of $NiMoO_4{\cdot}xH_2O$ pre-catalyst is $NiMoO_4{\cdot}H_2O$.

The pre-catalyst was then dissolved in alkaline solution to remove Mo species and generate $Ni(OH)_2$. In order to understand the detailed mechanisms governing the dissolution process, the dissolving process was monitored via in situ cryoTEM, with the composition of samples at corresponding dissolving time points studied by in situ Raman simultaneously (Figure 1c–h; Figure S4, Supporting Information). The initial rod-like morphology was basically maintained when $NiMoO_4{\cdot}H_2O$ pre-catalyst was just dipped into KOH solution (dissolving-2 min) (Figure 1c). The lattice spacing of 0.82 nm inside the nanorods was the same as before the reaction, but a small fraction of strip-like amorphous regions appeared at the edge of the rod and the width of the strips was only ≈0.8 nm. The peaks shown by in situ Raman of dissolving-2 min sample were basically unchanged with respect to the original sample, while a new peak appeared at 899 cm$^{-1}$, which could be attributed to free $MoO_4^{2-}$ in alkaline solution (Figure 1d).[13] These results indicate that the dissolving process of $NiMoO_4{\cdot}H_2O$ pre-catalyst first occurs at the crystal surfaces where the catalyst came into contact with alkaline solution.

With the increase of dissolving time to 10 min, the stripy amorphous regions developed into larger areas of disordered network, implying that the dissolution did not only happen near the crystal surface but was capable of continuously disintegrate the bulk structure of $NiMoO_4{\cdot}H_2O$ nanorods (Figure 1e). Among the amorphous network, a few denser sheets was observed (marked by the red arrows). The remaining crystalline regions still showed the lattice spacing of 0.82 nm (inset of the Figure 1e). The peak strength of free molybdate of this sample increased significantly in the Raman spectrum, while the peak strength of molybdate at 950 cm$^{-1}$ decreased (Figure 1f). There were two broad peaks at the low Raman shift positions of 300–350 and 463 cm$^{-1}$, which were attributed to the vibration of Ni–OH and Ni–O. The results indicate that some of the Ni sites exposed after the dissolving of Mo species and crystalline water to generate new Ni–OH and Ni–O bonds.[14]

When the reaction time of $NiMoO_4{\cdot}H_2O$ pre-catalyst and alkaline solution is extended to 20 min, only amorphous flocculus with low contrast (i.e., low density) in the cryoTEM image and no crystalline lattice could be detected in the sample (Figure 1g). Inset in Figure 1g is the fast Fourier transform (FFT) pattern of the image, which shows only vague diffraction signal from the vitreous ice, confirming the amorphousity of the flocculus. The corresponding Raman spectrum showed that the peak of molybdate totally disappeared and the $E_g$ and $A_{1g}$ lattice modes of $Ni(OH)_2$ were clearly identified at 314 and 451 cm$^{-1}$, respectively, that is, the $NiMoO_4{\cdot}H_2O$ pre-catalyst achieved a complete transformation to amorphous $Ni(OH)_2$ (nickel hydroxide), namely ANH.[15]

Energy dispersive spectroscopy (EDS) elemental mapping of ANH (Figure 1i–l) demonstrated that Mo element was almost lost, which are distinctly different from that in $NiMoO_4{\cdot}H_2O$ precatalyst (Figure S5, Supporting Information). In addition, negligible content of the Mo element suggested its absence within the ANH flocculus, indicating the leaching of Mo species in $NiMoO_4{\cdot}H_2O$. Atomic force microscopy (AFM) image and the corresponding height profiles of the ANH flocculus revealed a thickness of ≈0.8 nm (Figure 1m), illustrating the superthin character of ANH flocculus. These results confirmed the formation of superthin and amorphous $Ni(OH)_2$ flocculus from $NiMoO_4{\cdot}H_2O$ pre-catalyst through the destruction the bulk structure.

### 2.2. The Multistep Dissolution Mechanism of the Pre-Catalyst

In order to further investigate the dissolution process of $NiMoO_4{\cdot}H_2O$ pre-catalyst in 3D, we further conducted cryoET studies (**Figure 2**; Videos S1–S3, Supporting Information). Figure 2a–c, d–f, and g–i show 3D models reconstructed from the tomographic results of $NiMoO_4{\cdot}H_2O$ pre-catalyst dissolved for 0, 10, and 20 min, respectively, each viewed in three characteristic angles. The results confirm the rod-like morphology of the initial product (Figure 2a–c). After dissolving for 10 min (Figure 2d–f), the sample basically maintained the initial rod-like morphology while the outer amorphous zone was actually composed of ill-shaped nanolayers (in white). The regions in the amorphous network with higher density were confirmed to be thicker nanosheets (in green) and were distributed at different locations near the surface of the nanorods (inset in Figure 2d). By thoroughly examining the tomographic tilt series, weak crystalline lattice signals were detected for these nanosheets corresponding to $NiMoO_4{\cdot}H_2O$ (Figure S6, Supporting Information), indicating that these were $NiMoO_4{\cdot}H_2O$ crystalline sheets delaminated from the nanorods. EDS elemental mapping proved that Mo species were still uniformly distributed in the dissolving-10 min sample (Figure S7, Supporting Information). The ANH formed after 20 min of dissolving were confirmed to be in the form of flocculus (Figure 2g–i). It is worth mentioning that ANH was extremely sensitive to electron exposure and start to deform after being exposed to an electron dose of 30 e$^-$ Å$^{-2}$, while the dissolving-10 min samples can withstand an electron dose of more than 400 e$^-$ Å$^{-2}$, implying that the ANH flocculus are water-rich amorphous species. These observations suggest a multistep dissolution mechanism of $NiMoO_4{\cdot}H_2O$ pre-catalyst in which $NiMoO_4{\cdot}H_2O$ nanorods were exfoliated internally by alkali etching to form $NiMoO_4{\cdot}xH_2O$ nanosheets, and Mo species along with the remaining crystalline water further dissolved from these $NiMoO_4{\cdot}xH_2O$ nanosheets. As a result, the $NiMoO_4{\cdot}H_2O$ nanosheets became amorphous gradually. We envisage that the presence of crystalline water provides a path for the alkali solution to etch the internal structure. To confirm that hypothesis, we synthesized $NiMoO_4{\cdot}0.75H_2O$ and $NiMoO_4{\cdot}0.6H_2O$ by annealing $NiMoO_4{\cdot}H_2O$ in air (Figure S8, Supporting Information). The products exhibited almost the same crystal size and crystallinity compared of $NiMoO_4{\cdot}H_2O$ precatalyst as shown by PXRD and TEM (Figure S9,S10, Supporting Information). Both of the two controlling samples remained basically the original nano-rod morphology after the same treatment in alkali solution for 20 min, indicating that the dissolution rate was significantly slowed down after reducing the crystalline water (Figure S11, Supporting Information).

To further understand the mechanism of the multistep dissolution process, we conducted the density functional studies

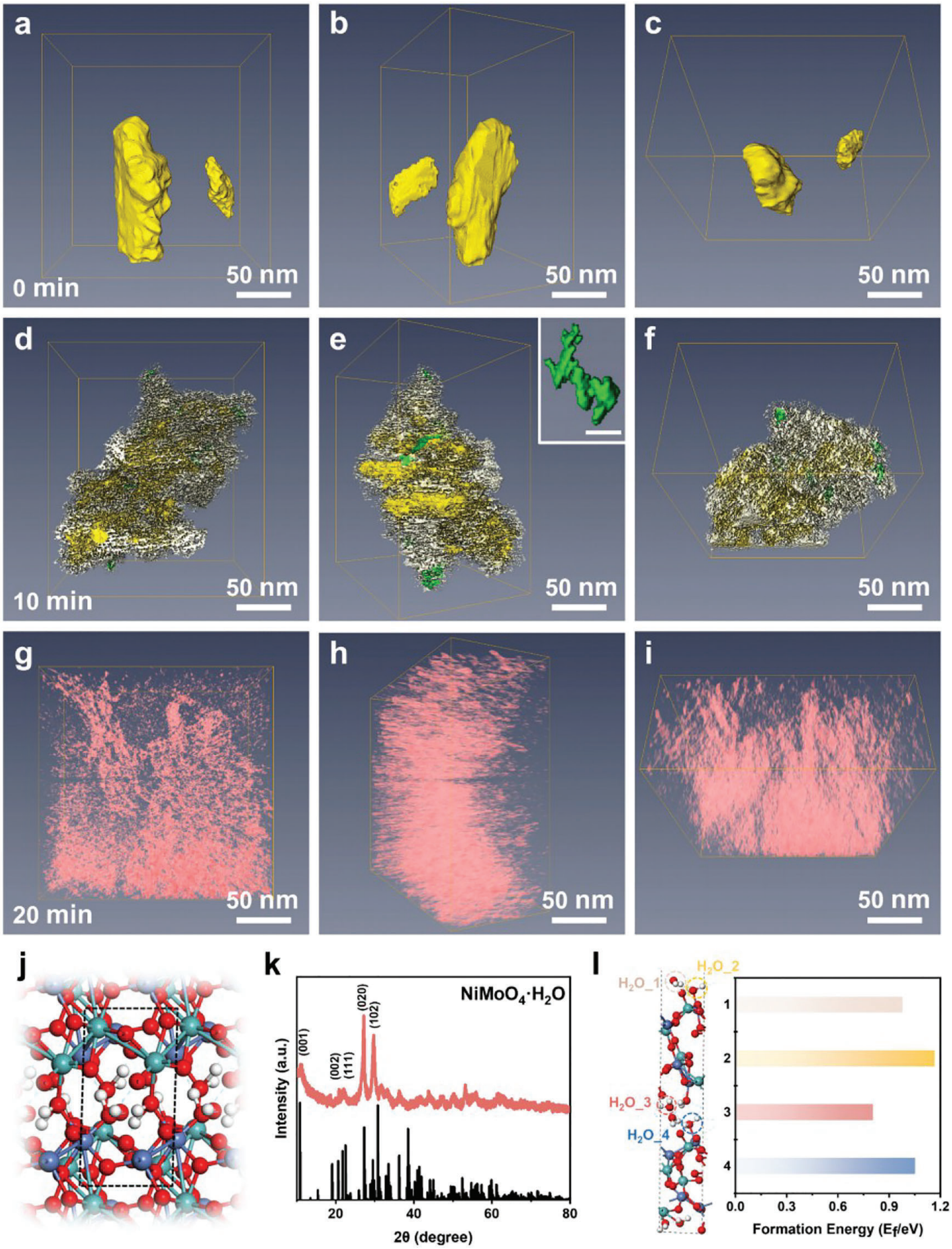

**Figure 2.** The multistep dissolution mechanism of the pre-catalyst visualized by cryoET. a-i) CryoET reconstructed 3D models of $NiMoO_4 \cdot H_2O$ dissolved in alkaline solution for a–c) 0 min, d–f) 10 min and g–i) 20 min, respectively, each in three different view angles. Bulk $NiMoO_4 \cdot H_2O$ crystals are in yellow, exfoliated $NiMoO_4 \cdot xH_2O$ nanosheets are in white and green, and ANH flocculus are in red. Inset of (e) shows the $NiMoO_4 \cdot xH_2O$ nanosheets delaminated from the nanorods, scale bar: 1 nm. j) Optimized crystal structure and corresponding k) simulated XRD pattern of $NiMoO_4 \cdot H_2O$. Ni species are blue, Mo as green, O as red, and H as white. The dashed blue lines between water molecules indicate hydrogen bond interactions. l) Optimized $NiMoO_4 \cdot H_2O$ (001) surface (left) and the corresponding crystalline water stripping formation energy (right). $H_2O\_1$ and $H_2O\_3$ represent surface and interlayer free water molecules, respectively; $H_2O\_2$ and $H_2O\_4$ represent water molecules bonding with Ni at the surface and between the crystalline layers, respectively.

on the structure of $NiMoO_4{\cdot}H_2O$. The crystal structure of $NiMoO_4{\cdot}H_2O$ (Space group: P1, a = 4.47 Å, b = 6.95 Å, c = 8.41 Å, $\alpha = 76.6°$, $\beta = 84.2°$, $\gamma = 74.5°$, see Supporting Information for the CIF file of the structure) was simulated based on our XRD experimental data and the corresponding PDF card (JCPDS no. 13–0128), as shown in Figure 2j,k. Due to the large amount of crystalline water, there is obvious hydrogen bonding between the crystals. The optimized $NiMoO_4{\cdot}H_2O$ (001) facet (a facet in parallel with the long axis of the nanorod with d-spacing of 0.82 nm) in Figure 2l indicated that the exposed surfaces tend to be layered structures constructed by hydrogen bonds. The subsequent calculation of the defect formation energy of crystalline water stripping showed that the free water molecules in the interlayer were more easily stripped than others. In other words, further stripping of free water between layers is conducive to the formation of layered $NiMoO_4{\cdot}xH_2O$ nanosheets.

To further simulate the stripping of Mo species, we used explicit water box molecules between $NiMoO_4{\cdot}H_2O$ surface slab (2 layers) with an area of 8.94 × 6.95 Å$^2$. Three water layers were applied as a solved model to minimize the size of simulated system. A total of 11 water molecular (with 1 $OH^-$and 1 $K^+$) were placed on $NiMoO_4{\cdot}H_2O$ surface with a water density of ≈1 g cc$^{-1}$. To equilibrate the waters interacting with the interface, we carried out 20 ps (time step is 1 fs) of molecular dynamics (MD) simulation at 298 K. The potential energies and temperature during the MD simulation are shown in Figure S12 (Supporting Information). The structure optimization after Mo species stripping showed that there was a lot of hydrogen bonding between molybdate and water molecules in alkalin solution. Single point energy calculation verified that the energy with Mo species stripping is 0.302 eV lower than that before stripping (Figure S13, Supporting Information). In other words, the stripping of Mo species in alkaline solution is thermodynamically favored.

In addition, X-ray absorption near-edge structure (XANES) and Fourier-transformed extended X-ray absorption fine structure (FT-EXAFS) have been carried out to further identify the electronic structure and local coordination environment of ANH and commercial $Ni(OH)_2$. The Ni K-edge XANES in Figure S14a (Supporting Information) revealed that the white line peak energy and intensity (black arrow) of ANH catalyst shifted to a higher energy with intensity also increased in comparison with that of commercial $Ni(OH)_2$, suggesting more Ni→O electron transfer in ANH catalyst.[16] Figure S14b (Supporting Information) shows the FT-EXAFS curves of ANH and commercial $Ni(OH)_2$. The peaks at 1.65 and 2.77 Å for both ANH and commercial $Ni(OH)_2$ can be assigned to Ni–O and Ni–Ni paths, respectively. The decreased intensity of the Ni–Ni peak for ANH suggests that the ANH has a lower Ni–Ni coordination number but the same Ni–O coordination number compared with those of commercial $Ni(OH_{)2}$, which is most likely due to Ni defects in the material. Furthermore, the X-ray Photoelectron Spectroscopy (XPS) of O 1s was carried out to investigate the oxygen vacancies (Figure S15, Supporting Information). The observed signal can be divided into three peaks $O_I$, $O_{II}$, and $O_{III}$ at 530.2, 531.4, and 532.1-539.9 eV, which are assigned to lattice oxygen, surface oxygen and absorbed $H_2O$ on the surface, respectively.[17] The higher percentage of surface oxygen ($O_{II}$ peak) of ANH is attributed to the Ni defects in the structure as suggested by the FT-EXAFS results and the more surface area of ANH.[17] These special structures of ANH may favor the $Ni^{2+}$ to $Ni^{3+}$ transformation.

To sum up, $NiMoO_4{\cdot}H_2O$ follows the multistep dissolution mechanism in the process of dissolving due to the containing of more crystalline water. The original compact and ordered structure of the catalyst is completely destroyed, forming loose flocculent amorphous $Ni(OH)_2$, which is conducive to the formation of active Ni sites in the oxidation reaction.

### 2.3. Electrochemical Performance

The oxidation process of ANH was investigated through potential-dependent in situ Raman spectroscopy, which is an ideal technique to monitor the oxidation state evolution from $Ni(OH)_2$ to NiOOH (**Figure 3**a). Well-defined commercial $Ni(OH)_2$ was used as a control (Figure 3b; Figure S16, Supporting Information). At low potentials (0-1.3 V), both ANH and commercial $Ni(OH)_2$ exhibited two peaks of $E_g$ and $A_{1g}$ lattice modes of $Ni(OH)_2$.[14,15] For ANH, a broad peak appeared at 470–600 cm$^{-1}$ as the applied potential was increased to 1.32 V, which illustrated the formation of NiOOH species.[18] When the applied potential was further increased to 1.34 V, two more peaks appeared at 483 and 561 cm$^{-1}$, respectively, which was attributed to the doublet peaks of NiOOH.[13,18] These peaks were retained as the potential was increased to 1.5 V. As a counterpart, commercial $Ni(OH)_2$ started to form a few NiOOH species merely when the potential was increased to 1.36 V or higher. To further verify this observation, we employed in situ XANES to obtain the electronic states of the as-prepared catalysts (Figure 3c). The normalized Ni K-edge XANES spectra of ANH and $Ni(OH)_2$ were collected for samples at open circuit potential (OCP) (notated as $Ni(OH)_2$-OCP) and after activating by cyclic voltammetry (CV) 5 cycles (notated as $Ni(OH)_2$-CV). The adsorption edge of ANH was positively shifted to higher energy after 5 cycles of activation, while the spectra of $Ni(OH)_2$-OCP and $Ni(OH)_2$-CV showed almost identical features, illustrating that the oxidation of Ni to form NiOOH species is much easier for ANH.[19] Both Raman and XAS results verified that the ANH was more likely to be oxidized at lower potential, which ensures the outstanding activity during UOR.

Then, the electrochemical performance of ANH catalyst in the three-electrode configuration was performed. The linear sweep voltammetry (LSV) was carried out in 1 м KOH and 1 м KOH + 0.33 M urea to evaluate their OER and UOR performance, respectively. The ANH catalyst achieved a low potential of 1.34 V at 100 mA cm$^{-2}$ while catalyzing UOR, which is ≈50 mV lower than that of OER (Figure S17, Supporting Information). As shown in Figure 3d; Figure S18 (Supporting Information), ANH catalyst also outperformed commercial $Ni(OH)_2$ (1.45 V at 100 mA cm$^{-2}$) during UOR, indicating that the Ni sites formed after the dissolving of Mo species and crystalline water possess high catalytic activity for UOR. The bare Ni foam displayed low current density, which excludes the substrate contribution to UOR performance. Moreover, ANH catalyst exhibited more than an order of magnitude higher current density at 1.4 V (640 mA cm$^{-2}$) than $Ni(OH)_2$ catalyst (55 mA cm$^{-2}$), which delivered one of the highest current density at 1.4 V compared with those of the reported catalyst for UOR (Table S2, Supporting Information).[3a,5,20]

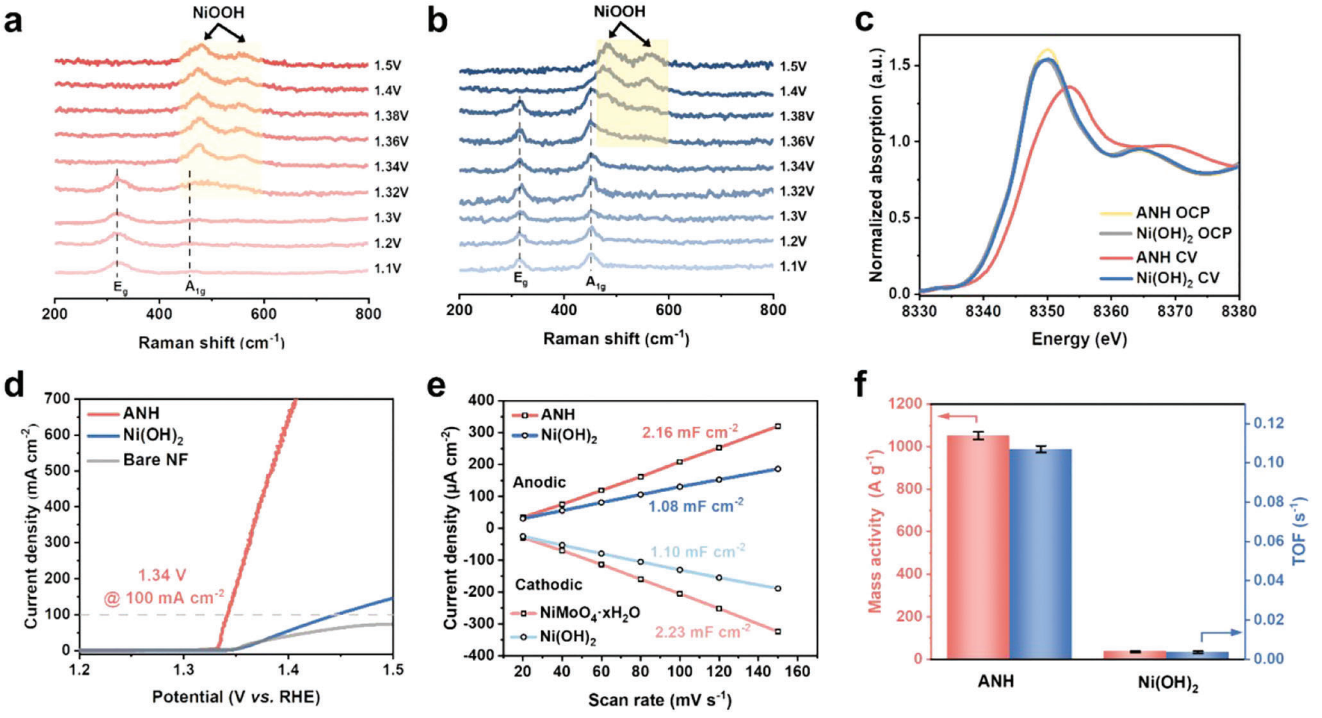

**Figure 3.** The evaluation of UOR activity. a,b) In situ Raman spectra obtained at constant potentials to display the evolution of ANH and $Ni(OH)_2$ in 1 м KOH during the electrochemical charging. c) In situ Ni K-edge XANES spectra of the ANH and $Ni(OH)_2$ electrodes in different electrochemistry stages. d) The UOR polarization curves, e) the measurements of ECSA and f) the mass-specific activities and TOFs of the different catalysts.

To obtain specific activity of ANH, the electrochemical surface area (ECSA) of catalysts was obtained by measuring double-layer capacitance in the non-Faradaic region (Figure 3e; Figure S19, Supporting Information). The ANH catalyst possesses both higher ECSA and ECSA-normalized specific activity. Furthermore, the loading mass was normalized to obtain the mass activity and calculated the turnover frequency (TOF) at each Ni site to evaluate the intrinsic activity. As shown in Figure 3f; Table S3 (Supporting Information), the mass activity of ANH was 30 times higher than that of $Ni(OH)_2$ catalyst at 1.4 V, while the TOF of ANH (0.107 $s^{-1}$ @1.4 V) was nearly 27 times higher than that of $Ni(OH)_2$ (0.004 $s^{-1}$ @1.4 V). Therefore, ANH catalyst shows a much higher intrinsic activity for UOR.

To gain the UOR kinetics, we further investigated the electrochemical impedance spectroscopy (EIS) with different catalysts. The Nyquist plots of the catalysts at 1.32 V was shown in Figure S20 and Table S3 (Supporting Information). The charge transfer resistance ($R_{ct}$) obtained from EIS was related to the UOR kinetics at catalysts/electrolyte interface. The smaller value of $R_{ct}$ obtained from ANH (4.3 Ω) than that of $Ni(OH)_2$ (26.3 Ω) further checks its exceptional UOR activity. Moreover, in situ time-resolved Fourier transform infrared (FTIR) was carried out to gain more insights into the UOR kinetics (Figure S21, Supporting Information). Both of the ANH and $Ni(OH)_2$ catalysts exhibited a vibration peak at 2168 $cm^{-1}$ during UOR, which can be attributed to $CNO^-$ intermediates.[21] With the increase of reaction time, the peak of $CNO^-$ intermediates became much more pronounced for ANH catalyst than that of $Ni(OH)_2$ catalyst, which reflects that the ANH catalyst has faster reaction kinetics as well.

We also evaluated the UOR performance and intrinsic activities of $NiMoO_4{\cdot}0.75H_2O$ and $NiMoO_4{\cdot}0.6H_2O$ catalysts after dissolving (named as 0.75-D and 0.6-D, respectively) (Figure S22 Supporting Information). ANH catalyst possessed both the best UOR activity and the ECSA-normalized specific activity than those of 0.75-D and 0.6-D. The TOF of ANH (0.107 $s^{-1}$ at 1.4 V) was nearly 10 and 15 times higher than that of 0.75-D (0.011 $s^{-1}$) and 0.6-D (0.007 $s^{-1}$), respectively. These results indicate that ANH catalyst formed through the multistep dissolution mechanism possesses the highest UOR activity compared to controls. In addition, we have synthesized amorphous $Ni(OH)_2$ catalyst following the method reported to evaluate the effect of amorphous structure on UOR performance.[22] TEM and PXRD were carried out to confirm the amorphous structure (Figure S23, Supporting Information). As shown in Figure S24 (Supporting Information), the potential at 100 mA $cm^{-2}$ (1.41 V) was reduced by 30 mV in comparison with the commercial well-crystallized $Ni(OH)_2$. The ANH catalyst also possessed both the highest ECSA (7.32 $cm^{-2}$) and specific activity. The results indicate that the amorphous structure is helpful to reduce the potential of UOR to a certain extent, but not enough to explain the outstanding UOR performance of ANH (reduced by 100 mV). Therefore, we attributed the outperforming performance to a synergic effect of the amorphous structure and the ultra-low thickness of the material. On one hand, the amorphous structure of ANH modified the coordination structure of Ni sites, thus enhanced the intrinsic activity of each Ni site. On the other hand, the superthin ANH flocculus expose rich active sites and benefits the formation of high valence Ni species in real-time catalysis, which facilitates the charge transfer process and thus improves the UOR performance.

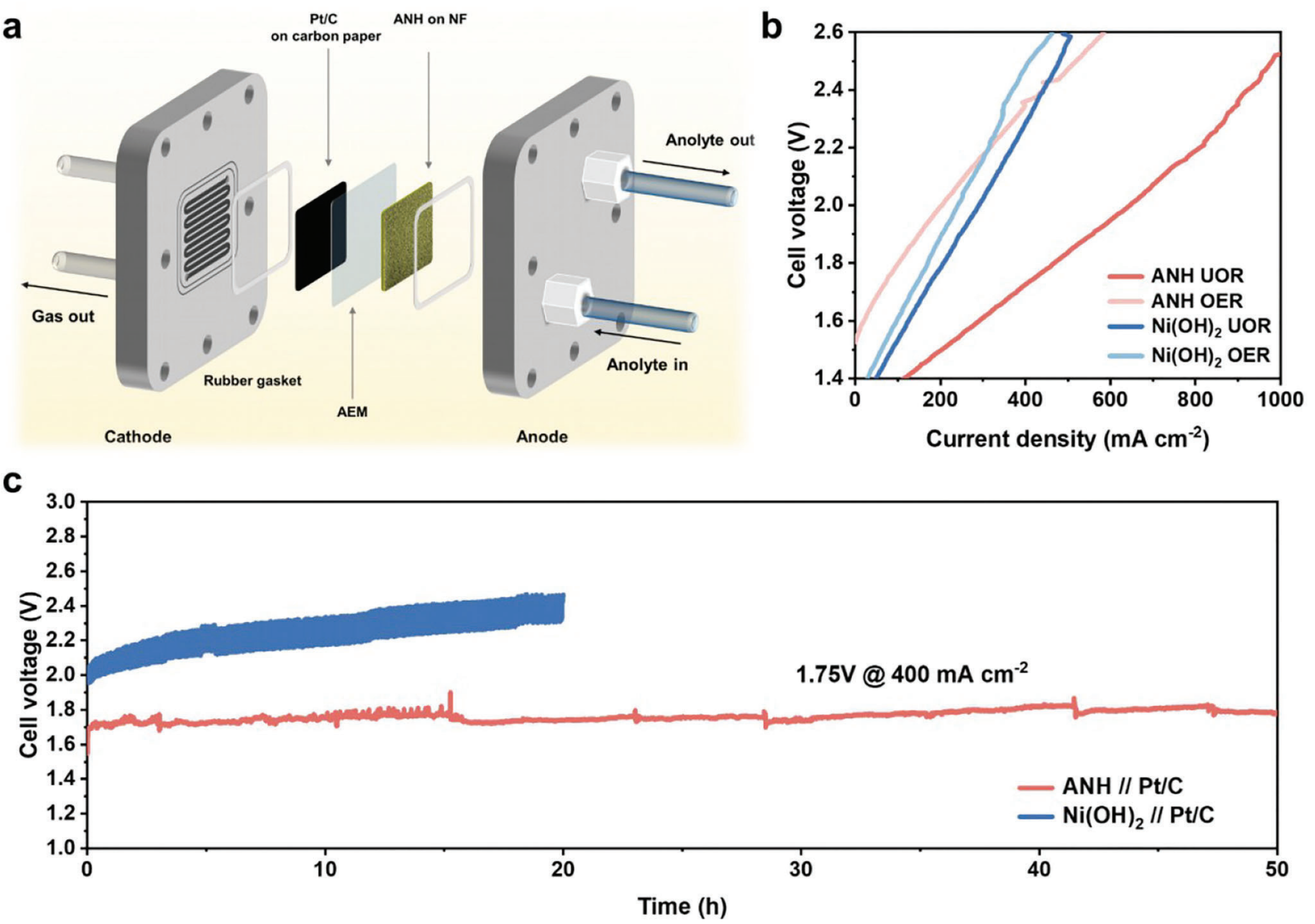

**Figure 4.** OER replacement by the UOR in urea-assisted AEM electrolyzer for hydrogen production. a) Schematic of the urea-assisted AEM electrolyzer. b) Comparison of LSVs for UOR//HER and OER//HER using an ANH electrode (red) and a $Ni(OH)_2$ electrode (blue) as an anode, respectively. c) Durability of the urea-assisted AEM electrolyzer at 400 mA cm$^{-2}$ for 50 h at 50 °C in 1 M KOH with 0.33 M urea.

Beside the superior UOR activity, the ANH catalyst also possesses excellent stability with negligible potential increase for 100 h at a constant current density of 50 mA cm$^{-2}$ (Figure S25, Supporting Information). In sum, the ANH catalyst possesses superior UOR activity relative to the dissolution products of less hydrated $NiMoO_4{\cdot}xH_2O$ as well as crystalline $Ni(OH)_2$.

### 2.4. Urea-Assisted Anion-Exchange Membrane Electrolyzer for $H_2$ Production

The remarkable catalytic performance of ANH during UOR process prompted us to apply it to an urea-assisted anion-exchange membrane (AEM) electrolyzer, which was constructed by ANH//NF and Pt/C//GDL as the anode and the cathode, respectively (**Figure 4**a; Figure S26, Supporting Information). Figure 4b shows the polarization curves of ANH and $Ni(OH)_2$ in 1 M KOH with and without 0.33 M urea. As expected, the ANH catalyst reached the UOR current density of 650 mA cm$^{-2}$ at the cell potential of 2 V, which is higher than that of $Ni(OH)_2$ catalyst (290 mA cm$^{-2}$) In addition, the urea electrolysis of ANH required less energy input than water electrolysis, which illustrates the energy-saving superiority of ANH to drive UOR for $H_2$ production. The ANH catalyst also displayed high stability in the urea-assisted AEM electrolyzer. The urea-assisted electrolyzer delivered 400 mA cm$^{-2}$ at ≈1.75 V without no appreciable increase in the voltage over 50 h, indicating its potential for large-scale energy-saving $H_2$ degeneration at harsher conditions (Figure 4c).

## 3. Conclusion

In summary, superthin and amorphous $Ni(OH)_2$ flocculus catalyst was fabricated through a multistep dissolution mechanism in alkali solution. The in situ cryoTEM, multi-angle cryoET and in situ Raman, along with theoretical calculations, revealed the process of the multistep dissolution: 1) $NiMoO_4{\cdot}xH_2O$ nanosheets are exfoliated from $NiMoO_4{\cdot}H_2O$ nanorods by the loss of crystalline water in alkali solution; 2) the remaining crystalline water and Mo species are further dissolved from the $NiMoO_4{\cdot}xH_2O$ nanosheets. Thus, the initial morphology of $NiMoO_4{\cdot}H_2O$ nanorods is totally collapsed and successfully reduced the oxidation potential of $Ni^{2+}$ to 1.32 V. The ANH catalyst exhibits more than an order of magnitude higher current density (640 mA cm$^{-2}$), 30 times higher mass activity, 27 times higher

TOF than those of $Ni(OH)_2$ catalyst. This work provides an effective avenue to develop amorphous electrocatalysts to boost the UOR activity.

## Supporting Information

Supporting Information is available from the Wiley Online Library or from the author.

## Acknowledgements

This work was supported by NSFC (21875042, 22279019, 22205038), STCSM (21DZ1207102, 21DZ1207103), National Key Research and Development Program of China (Grants No. 2022YFA1503101) and Shanghai Pujiang Program. This work has also benefited from the 1W1B Beamline at Being Synchrotron Radiation Facility and the authors thank Prof. Lirong Zheng for the assistance in the XAS measurements. The authors also appreciate the Shiyanjia Lab (www.shiyanjia.com) for the XPS tests.

## Conflict of Interest

The authors declare no conflict of interest.

## Data Availability Statement

The data that support the findings of this study are available from the corresponding author upon reasonable request.

## Keywords

amorphous nickle hydroxide, cryogenic electron tomography, electrocatalysis, multistep dissolution mechanism, urea oxidation reaction

Received: February 17, 2023
Revised: April 4, 2023
Published online:

---

[1] a) N. T. Suen, S. F. Hung, Q. Quan, N. Zhang, Y. J. Xu, H. M. Chen, *Chem. Soc. Rev.* **2017**, *46*, 337; b) Y. Bai, Y. Wu, X. Zhou, Y. Ye, K. Nie, J. Wang, M. Xie, Z. Zhang, Z. Liu, T. Cheng, C. Gao, *Nat. Commun.* **2022**, *13*, 6094; c) D. Zhu, L. Wang, M. Qiao, J. Liu, *Chem. Commun. (Camb.)* **2020**, *56*, 7159; d) Z. W. Seh, J. Kibsgaard, C. F. Dickens, I. Chorkendorff, J. K. Nørskov, T. F. Jaramillo, *Science* **2017**, *355*, eaad4998.

[2] a) T. Wang, L. Tao, X. Zhu, C. Chen, W. Chen, S. Du, Y. Zhou, B. Zhou, D. Wang, C. Xie, P. Long, W. Li, Y. Wang, R. Chen, Y. Zou, X.-Z. Fu, Y. Li, X. Duan, S. Wang, *Nat. Catal.* **2021**, *5*, 66; b) Y. Wang, C. Xie, Z. Zhang, D. Liu, R. Chen, S. Wang, *Adv. Funct. Mater.* **2018**, *28*, 1703363.

[3] a) J. Li, J. Li, T. Liu, L. Chen, Y. Li, H. Wang, X. Chen, M. Gong, Z. P. Liu, X. Yang, *Angew Chem Int Ed Engl* **2021**, *60*, 26656; b) K. Ye, G. Wang, D. Cao, G. Wang, *Top Curr Chem (Cham)* **2018**, *376*, 42.

[4] H. Sun, J. Liu, G. Chen, H. Kim, S. Kim, Z. Hu, J.-M. Chen, S.-C. Haw, F. Ciucci, W. Jung, *Small Methods* **2022**, *6*, 2101017.

[5] S.-K. Geng, Y. Zheng, S.-Q. Li, H. Su, X. Zhao, J. Hu, H.-B. Shu, M. Jaroniec, P. Chen, Q.-H. Liu, S.-Z. Qiao, *Nat. Energy* **2021**, *6*, 904.

[6] D. Zhu, H. Zhang, J. Miao, F. Hu, L. Wang, Y. Tang, M. Qiao, C. Guo, *J. Mater. Chem. A* **2022**, *10*, 3296.

[7] W. Chen, L. Xu, X. Zhu, Y. C. Huang, W. Zhou, D. Wang, Y. Zhou, S. Du, Q. Li, C. Xie, L. Tao, C. L. Dong, J. Liu, Y. Wang, R. Chen, H. Su, C. Chen, Y. Zou, Y. Li, Q. Liu, S. Wang, *Angew Chem Int Ed Engl* **2021**, *60*, 7297.

[8] a) K. Hu, S. Jeong, G. Elumalai, S. Kukunuri, J.-i. Fujita, Y. Ito, *ACS Appl. Energy Mater.* **2020**, *3*, 7535; b) Y. Liang, Q. Liu, A. M. Asiri, X. Sun, *Electrochim. Acta* **2015**, *153*, 456; c) D. Yang, L. Yang, L. Zhong, X. Yu, L. Feng, *Electrochim. Acta* **2019**, *295*, 524; d) L. An, Y. Zhang, R. Wang, H. Liu, D. Gao, Y. Q. Zhao, F. Cheng, P. Xi, *Nanoscale* **2018**, *10*, 16539; e) G. Fu, X. Kang, Y. Zhang, X. Yang, L. Wang, X.-Z. Fu, J. Zhang, J.-L. Luo, J. Liu, *Nano-Micro Lett.* **2022**, *14*, 200.

[9] X. Liu, J. Meng, K. Ni, R. Guo, F. Xia, J. Xie, X. Li, B. Wen, P. Wu, M. Li, J. Wu, X. Wu, L. Mai, D. Zhao, *Cell Rep. Phys. Sci.* **2020**, *1*, 100241.

[10] a) L. Jin, R. Ji, H. Wan, J. He, P. Gu, H. Lin, Q. Xu, J. Lu, *ACS Catal.* **2022**, *13*, 837; b) S. Anantharaj, S. Noda, *Small* **2020**, *16*, 1905779; c) Y. Zhai, X. Ren, J. Yan, S. Liu, *Small Struct.* **2021**, *2*, 2000096.

[11] H. Wan, J. Jiang, X. Ji, L. Miao, L. Zhang, K. Xu, H. Chen, Y. Ruan, *Mater. Lett.* **2013**, *108*, 164.

[12] O. M. Popovych, I. M. Budzulyak, V. O. Yukhymchuk, S. I. Budzulyak, D. I. Popovych, *Fuller. Nanotub. Carbon Nanostructures* **2021**, *29*, 1009.

[13] R. N. Durr, P. Maltoni, H. Tian, B. Jousselme, L. Hammarstrom, T. Edvinsson, *ACS Nano* **2021**, *15*, 13504.

[14] J. L. Bantignies, S. Deabate, A. Righi, S. Rols, P. Hermet, J. L. Sauvajol, F. Henn, *J. Phys. Chem. C* **2008**, *112*, 2193.

[15] D. S. Hall, D. J. Lockwood, S. Poirier, C. Bock, B. R. MacDougall, *J. Phys. Chem. A* **2012**, *116*, 6771.

[16] a) L. Zhu, Y. Sun, H. Zhu, G. Chai, Z. Yang, C. Shang, H. Ye, B. H. Chen, A. Kroner, Z. Guo, *ACS Catal.* **2022**, *12*, 8104; b) A. Grimaud, O. Diaz-Morales, B. Han, W. T. Hong, Y. L. Lee, L. Giordano, K. A. Stoerzinger, M. T. M. Koper, Y. Shao-Horn, *Nat. Chem.* **2017**, *9*, 457.

[17] V. M. Jiménez, A. Fernández, J. P. Espinós, A. R. González-Elipe, *J. Electron Spectrosc. Relat. Phenom.* **1995**, *71*, 61.

[18] V. Vedharathinam, G. G. Botte, *Electrochim. Acta* **2013**, *108*, 660.

[19] Y. Lin, H. Wang, C.-K. Peng, L. Bu, C.-L. Chiang, K. Tian, Y. Zhao, J. Zhao, Y.-G. Lin, J.-M. Lee, L. Gao, *Small* **2020**, *16*, 2002426.

[20] a) H. Sun, L. Li, H. C. Chen, D. Duan, M. Humayun, Y. Qiu, X. Zhang, X. Ao, Y. Wu, Y. Pang, K. Huo, C. Wang, Y. Xiong, *Kexue Tongbao (Foreign Lang. Ed.)* **2022**, *67*, 1763; b) Z. Wang, Y. Hu, W. Liu, L. Xu, M. Guan, Y. Zhao, J. Bao, H. Li, *Chemistry* **2020**, *26*, 9382; c) Z. Ji, J. Liu, Y. Deng, S. Zhang, Z. Zhang, P. Du, Y. Zhao, X. Lu, *J. Mater. Chem. A* **2020**, *8*, 14680; d) J. Xie, L. Gao, S. Cao, W. Liu, F. Lei, P. Hao, X. Xia, B. Tang, *J. Mater. Chem. A* **2019**, *7*, 13577; e) L. Wang, Y. Zhu, Y. Wen, S. Li, C. Cui, F. Ni, Y. Liu, H. Lin, Y. Li, H. Peng, B. Zhang, *Angew Chem Int Ed Engl* **2021**, *60*, 10577; f) J.-Y. Zhang, T. He, M. Wang, R. Qi, Y. Yan, Z. Dong, H. Liu, H. Wang, B. Y. Xia, *Nano Energy* **2019**, *60*, 894; g) H. Sun, W. Zhang, J.-G. Li, Z. Li, X. Ao, K.-H. Xue, K. K. Ostrikov, J. Tang, C. Wang, *Appl. Catal. B* **2021**, *284*, 119740; h) S. A. Patil, S. Cho, Y. Jo, N. K. Shrestha, H. Kim, H. Im, *Chem. Eng. J.* **2021**, *426*, 130773; i) Z. Wang, W. Liu, Y. Hu, M. Guan, L. Xu, H. Li, J. Bao, H. Li, *Appl. Catal. B* **2020**, *272*, 118959; j) J. Cao, H. Li, R. Zhu, L. Ma, K. Zhou, Q. Wei, F. Luo, *J. Alloys Compd.* **2020**, *844*, 155382; k) L. Sha, K. Ye, J. Yin, K. Zhu, K. Cheng, J. Yan, G. Wang, D. Cao, *Chem. Eng. J.* **2020**, *381*, 122603.

[21] L. Zhang, L. Wang, H. Lin, Y. Liu, J. Ye, Y. Wen, A. Chen, L. Wang, F. Ni, Z. Zhou, S. Sun, Y. Li, B. Zhang, H. Peng, *Angew. Chem. Int. Ed. Engl.* **2019**, *58*, 16820.

[22] S. Chakrabarty, I. Offen-Polak, T. Y. Burshtein, E. M. Farber, L. Kornblum, D. Eisenberg, *J. Solid State Electrochem.* **2020**, *25*, 159.